The Astrophysical Journal, 765:129 (13pp), 2013 March 10 doi:10.1088/0004-637X/765/2/129

TESTING 24 μm AND INFRARED LUMINOSITY AS STAR FORMATION TRACERS FOR GALACTIC STAR-FORMING REGIONS

Nalin Vutisalchavakul and Neal J. Evans II
The University of Texas at Austin, Department of Astronomy, 2515 Speedway, Stop C1400 Austin, TX 78712-1205, USA
Received 2012 May 9; accepted 2013 January 15; published 2013 February 26

ABSTRACT

We have tested some relations for star formation rates used in extragalactic studies for regions within the Galaxy. In nearby molecular clouds, where the initial mass function is not fully sampled, the dust emission at 24 μm greatly underestimates star formation rates (by a factor of 100 on average) when compared to star formation rates determined from counting young stellar objects. The total infrared emission does no better. In contrast, the total far-infrared method agrees within a factor of two on average with star formation rates based on radio continuum emission for massive, dense clumps that are forming enough massive stars to have $L_{\rm TIR}$ exceed $10^{4.5}$ $L_{\odot}$. The total infrared and 24 μm also agree well with each other for both nearby, low-mass star-forming regions and the massive, dense clump regions.

Key words: dust, extinction – galaxies: ISM – infrared: ISM – ISM: clouds – stars: formation

Online-only material: color figures

1. INTRODUCTION

Star formation is a fundamental process in the formation and evolution of galaxies (Kennicutt 1998b; Hopkins 2004; Bigiel et al. 2008; Gao & Solomon 2004). A unified picture of star formation across different scales and types of regions would benefit from unified measures of star formation rates (Krumholz et al. 2011, 2012; Schruba et al. 2011; Shi et al. 2011; Kennicutt 1998a). The most direct way to measure the rate of star formation is to count stars of a known age and mass. Because most galaxies are too far away for individual star-forming regions to be resolved, alternative measures of star formation rates have been developed.

Many different methods have been used to estimate the star formation rate (SFR) in galaxies (Kennicutt 1998b, hereafter K98). Commonly used tracers include continuum UV emission, recombination lines of hydrogen and other atomic species, total infrared luminosity ($L_{\rm TIR}$), monochromatic infrared emission, and radio emission (Kennicutt 1998b; Kennicutt et al. 2003, 2009; Calzetti et al. 2007, 2010; Pérez-González et al. 2006; Murphy et al. 2011; Kinney et al. 1993; Condon 1992). Each of these indicators traces star formation in somewhat different ways, averaging over different timescales (e.g., Kennicutt & Evans 2012). UV continuum emission in the wavelength range of 125–250 nm directly measures radiation from high-mass stars, with peak contributions from stars of several $M_{\odot}$; consequently, it can average SFR over 10–200 Myr. Hydrogen recombination lines, such as Hα, or free–free radio continuum emission trace H II regions surrounding high-mass stars ($M > 15\ M_{\odot}$), with a peak contribution from $M = 30$ to 40 $M_{\odot}$; thus, they average SFR over only 3–10 Myr (Kennicutt & Evans 2012 and references therein).

Most studies of star formation in galaxies use UV continuum or optical lines (e.g., Bigiel et al. 2008; Kinney et al. 1993; Salim et al. 2007; Hao et al. 2011). However, optical emission can be strongly affected by dust extinction, and the UV continuum is even more sensitive to extinction (Calzetti et al. 1994; Hao et al. 2011; Buat et al. 2005; Burgarella et al. 2005). The recombination lines trace only very massive stars, so they are sensitive to assumptions about the initial mass function (IMF; see Figure 1 in Chomiuk & Povich 2011).

As supplements to UV and optical tracers, IR fluxes have been used to study SFR in regions that are obscured by dust (Calzetti et al. 2007, 2010; Pérez-González et al. 2006; Kennicutt et al. 2009). Infrared dust emission traces the stellar luminosity that has been absorbed by dust and re-emitted in the infrared (K98; Calzetti et al. 2007). It is less biased toward the highest mass stars and hence less sensitive to the IMF. If all the photons inside star-forming regions get absorbed by dust, then the total infrared emission from dust ($L_{\rm TIR}$) should trace the total luminosity of the stars. One problem with using $L_{\rm TIR}$ to trace star formation is that sources other than young stars, such as older stars or active galactic nuclei, can contribute to heating the dust. For galaxies less active in star formation, a significant amount of dust heating can come from the general interstellar radiation field, arising from older stellar populations (K98; Draine et al. 2007). In that case, $L_{\rm TIR}$ would trace emission that is not relevant to the current star formation.

Monochromatic IR emission has also been widely used. One particularly widely used tracer is the 24 μm continuum emission (Calzetti et al. 2007; Wu et al. 2005a; Rieke et al. 2009; Alonso-Herrero et al. 2006; Helou et al. 2004). In principle, 24 μm emission has the advantage over $L_{\rm TIR}$ that it requires quite warm dust. In active star-forming regions, the warm dust is more intimately associated with the forming stars. The diffuse part of the interstellar medium that has been heated by the average interstellar radiation field should be at a comparatively low temperature and should not emit much in the 24 μm wavelength band compared to the emission from high-mass star-forming regions. Stronger radiation fields from high-mass stars can heat the dust to higher temperatures over a larger region; therefore, 24 μm emission should be a good tracer for high-mass star-forming regions with less contamination from non-star-forming sources.

There are several studies of how emission from non-star-forming sources compares to emission relevant to star formation in the 24 μm wavelength (Rahman et al. 2011; Verley et al. 2009; Draine et al. 2007). Draine et al. showed from fitting dust models to numbers of galaxies that for galaxies with high star formation

rates (starburst galaxies), the main contribution to the 24 μm emission comes from photodissociation regions associated with high-mass stars. For high-mass star-forming regions, 24 μm emission should be a good tracer of SFR. Observations of nearby galaxies show strong concentrations of 24 μm emission toward H II regions, but with a diffuse component.

Unifying studies of star formation in other galaxies with studies within the Milky Way can be mutually illuminating. Chomiuk & Povich (2011) have compared tracers of SFR on global scales and found a potential discrepancy of a factor of two between extragalactic relations applied to the Milky Way as a whole and more direct measures of the Milky Way SFR. Our goal is to test extragalactic relations on still smaller scales of individual clouds and dense clumps.

Images of the Galactic plane at 24 μm are available from MIPS on *Spitzer* from the infrared survey of the plane of the Milky Way (MIPSGAL; Carey et al. 2009) and at 25 μm from *Infrared Astronomical Satellite* (*IRAS*). If these could be used to measure star formation rates in regions of our Galaxy, it would be very useful. The goal of this paper is to test the limits of applicability of the extragalactic relations for regions within our Galaxy. Since we can observe star-forming regions in the Milky Way in more detail, testing extragalactic SFR relations on nearby regions can also provide some perspective on the use of such relations in other galaxies.

In order to test how well 24 μm emission can trace SFR, another method for tracing SFR is needed for comparison. We tie our measurements to those in nearby clouds, where we can count young stellar objects (YSOs) of a certain age. These provide a completely independent and reasonably accurate measure of the SFR. These nearby clouds are not forming high-mass stars, which means that the IMF is not fully sampled in these regions. Since one of the assumptions in deriving SFR from IR emission is that the IMF is fully sampled in the regions, studying the use of IR tracers in these nearby clouds can tell us about the effect of undersampling the IMF on SFR calibration. We then extend the study to regions forming massive stars. These regions are at larger distances than the nearby clouds, and counting individual YSOs in these regions as a measure of SFR is not feasible. With the lack of a direct method of measuring SFR, we instead compared SFR measured from 24 μm, $L_{\rm TIR}$, and radio continuum emission. In Section 2, we describe the sample of star-forming regions used in the study. In Section 3, we describe how the SFR was calculated for a sample of nearby molecular clouds. In Section 4, we consider high-mass star-forming regions using samples of massive, dense clumps from Wu et al. (2010). The resulting comparison of all the SFRs in this study is described in Section 5, and we summarize the results in Section 6.

2. THE SAMPLE

Two groups of sources were included in this study. The first group consists of nearby molecular clouds with evidence of low-mass star formation. This group has the advantage of having an independent estimate of the SFR from counting YSOs. The second group consists of massive dense clumps with evidence of high-mass star formation. This group does not have SFRs from YSO counting, but it is more representative of the star formation regions that might be seen in other galaxies.

The first group consists of 20 clouds within 1 kpc of the Sun, in the structure known as the Gould Belt (GB). They have data from *Spitzer* Legacy programs and ancillary data (Evans et al. 2003, core to disk (c2d); and L. E. Allen et al., in preparation, GB). The clouds are listed in Table 1, along with their distances. All the clouds have been observed in all IRAC (3.6, 4.5, 5.6, 8.0 μm) and MIPS bands (24, 70, 160 μm), using the same procedures and data reduction methods. YSOs were identified and categorized into their spectral energy distribution (SED) classes (Class I, Flat, Class II, and Class III) using the spectral index following the criteria from Greene et al. (1994). The details on identifying YSOs and calculating SFR in these clouds can be found in Evans et al. (2009) and Heiderman et al. (2010). We also make use of data from the *IRAS* data archive for assessing the large-scale emission from the clouds.

The second group contains massive dense clumps with evidence of high-mass star formation, selected from Wu et al. (2010). This sample is a subsample of a large survey by Plume et al. (1997) of regions associated with water masers, which are indicators of an early phase of massive star formation, most of which contain compact or ultracompact H II regions. These clumps have characteristic densities from CS excitation of about 10^6 cm^{-3} (Plume et al. 1997). The mean and median virial masses are 5300 and 2700 $M_\odot$, respectively. Most of these clumps have been observed in many molecular line transitions, such as CS lines (Plume et al. 1992, 1997; Shirley et al. 2003), HCN $J = 1 \rightarrow 0$ and $J = 3 \rightarrow 2$ (Wu et al. 2010), and HCO^+ and several others (Reiter et al. 2011). Some of the clumps have also been observed in 350 μm dust continuum emission by Mueller et al. (2002), who also tabulated *IRAS* data.

3. ANALYSIS OF THE REGIONS FORMING LOW-MASS STARS

Emission at 24 μm has been used in many extragalactic studies as a star formation tracer. A number of studies have derived an expression for the SFR as a function of the 24 μm emission [SFR(24 μm)] (Calzetti et al. 2007; Alonso-Herrero et al. 2006; Rieke et al. 2009; Wu et al. 2005a; Zhu et al. 2008; Relaño et al. 2007; Pérez-González et al. 2006). Various calibrations of SFR(24 μm) are compared in Calzetti et al. (2010). Our goal is to test these relations by comparing the SFR using 24 μm emission with the SFR using YSO counting (Evans et al. 2009; Heiderman et al. 2010).

The YSO counting method uses the following equation:

$$\mathrm{SFR(YSO\ count)} = N(\mathrm{YSOs})\langle M_* \rangle / t_{\rm excess}. \quad (1)$$

Assuming an average stellar mass of $\langle M_* \rangle = 0.5\,M_\odot$ and an average time for YSOs to have an infrared excess of $t_{\rm excess} = 2$ Myr, the SFRs were calculated by Evans et al. (2009) and Heiderman et al. (2010). The average mass was chosen to be consistent with IMF studies (Chabrier 2003; Kroupa 2002) and consistent with an average mass for some clouds although there may be variations between clouds (Evans et al. 2009). They are collected in Table 1. The largest source of uncertainty is the lifetime of the infrared excess (perhaps ± 1 Myr).

3.1. 24 μm Emission from YSOs

We now compare the SFRs calculated from counting YSOs [SFR(YSO count)] to the SFRs calculated using SFR(24 μm). Since 24 μm emission comes from dust that has been heated by stellar radiation and does not require high-energy photons, it may be able to pick up the SFR of even low-mass YSOs.

The first step was to calculate the total 24 μm emission coming from all the YSOs in each cloud. The flux densities at 24 μm for individual YSOs were extracted from databases and summed over all the YSOs in individual clouds. The resulting

Table 1
SFRs for the c2d and Gould Belt Clouds

Cloud	Distance (pc)	NYSOs	YSO 24 μm Flux (Jy)	SFR (YSO, 24 μm) ($M_\odot$ Myr^{-1})	SFR (YSO count) ($M_\odot$ Myr^{-1})	SFR(YSO count)/SFR(YSO, 24 μm)
Cha II	178	24	7.93	0.0066	6.0	910
Lup[a]	150	93	9.45	0.0057	23	4000
Oph	125	290	94.2	0.031	73	2400
Per	250	385	77.1	0.090	96	1100
Ser	260	224	56.7	0.073	57	770
Aur[b]	300	173	26.5	0.048	43	900
Cep	300	118	24.5	0.045	30	670
Cha III	200	4	0.254	0.00038	1.0	2600
Cha I	200	89	...	...	22	...
CrA	130	41	11.9	0.0054	10	1900
IC 5146[c]	950	131	16.9	0.25	33	130
Lup VI	150	45	6.67	0.0042	11	2600
Lup V	150	43	5.14	0.0033	11	3300
Mus	160	12	0.839	0.00075	3.0	4000
Sco	130	10	8.88	0.0042	2.5	600

Notes.
[a] Combined Lup I, Lup III, and Lup IV.
[b] Combined Aur and Aur N.
[c] Combined IC 5146E and IC 5146NW.

total YSO flux for each cloud is shown in Table 1. Using the distances to the clouds (Heiderman et al. 2010; updated distances can be found in M. M. Dunham et al., in preparation), the 24 μm luminosity can be calculated from the total 24 μm flux density.

From the total 24 μm emission from YSOs, we computed SFR(YSO, 24 μm). The relation for SFR(24 μm) that we used in this study came from the work of Calzetti et al. (2007), who adopted the Starburst99 stellar synthesis model and Kroupa's IMF (Kroupa 2001) in the calibration. Kroupa's IMF has been used in many studies for calibrating SFR; it has the form and stellar mass range described by (Chomiuk & Povich 2011; Kennicutt et al. 2009; Murphy et al. 2011)

$$\psi(\log(m)) \propto m^{-0.3} (0.1 \leqslant m \leqslant 0.5\, M_\odot),$$

$$\psi(\log(m)) \propto m^{-1.3} (0.5 \leqslant m \leqslant 100\, M_\odot).$$

Calzetti et al. (2007) use Kroupa's IMF but with an upper mass limit of 120 $M_\odot$. The SFR(24 μm) is

$$\mathrm{SFR}(M_\odot\ \mathrm{yr}^{-1}) = 1.27 \times 10^{-38} [L_{24\,\mu\mathrm{m}}(\mathrm{erg\ s}^{-1})]^{0.8850}, \quad (2)$$

where $L_{24\,\mu\mathrm{m}}$ is the total 24 μm luminosity per unit frequency times the frequency (νL_ν). The calculated SFRs for each cloud are as shown in Table 1.

It is clear that SFR(YSO, 24 μm) vastly underestimates SFR(YSO count). The mean ratio of SFR(YSO count) to SFR(YSO, 24 μm) is 1867 ± 1335.

3.2. Total 24 μm Emission

Since the relation in Equation (2) was derived for extragalactic star formation, where individual YSOs are not resolved, we should expect the detected flux to be contributed from diffuse emission as well as from point sources. In this section, we consider the total emission, which includes diffuse as well as point-source emission in SFR(24 μm).

To compare SFR from the total 24 μm emission with the SFR from YSO counting, the calculations have to come from the same area of the clouds. Boundaries for each cloud used for identifying YSOs were chosen using contours from extinction maps. Therefore, we chose the same boundaries for calculating diffuse emission. All clouds' boundaries were chosen to be extinction contours of $A_V = 2$. The exceptions are Serpens and Ophiuchus, for which the c2d survey extended down to $A_V = 6$ and $A_V = 3$, respectively (Evans et al. 2009). The total flux used to calculate the SFR should also be emission only from the clouds themselves. Images that cover the area inside the cloud's boundary can still contain foreground and background emission not associated with the clouds. To include only emission from the clouds, we subtracted background emission. To do this, we needed large-scale images that cover not only the area of the cloud defined by extinction contours but also the area surrounding the contour boundaries. MIPS images from the *Spitzer* survey have good spatial resolution but lack the area coverage needed for background estimations. Therefore, we chose to use *IRAS* images for our diffuse emission analysis.

IRAS observed 96% of the sky in four bands (12, 25, 60, 100 μm). We used 25 μm *IRAS* images from the Improved Reprocessing of the IRAS Survey (IRIS) obtained from the Infrared Processing and Analysis Center (IPAC) as a substitute for 24 μm data. First, the total flux densities inside contour boundaries were calculated for each cloud. We then chose a "sky annulus" for each cloud separately by choosing an area surrounding the cloud's boundary while avoiding any extended emission that seemed to be connected to the cloud. The background level was estimated by summing over the flux inside the sky annulus divided by the total number of pixels to estimate the background value per pixel (Jy pix^{-1}). The total flux inside contour boundaries minus the background flux (background flux = average background level per pixel $\times$ number of pixels inside the boundary) gave the actual flux from the clouds. The 25 μm emission coming from the clouds themselves turns out to be very small compared to the foreground/background emission. The 25 μm luminosities calculated from the background-subtracted flux for all the c2d and Gould Belt

Table 2
SFRs from Diffuse Emission of c2d and Gould Belt Surveys

Cloud	Dis (pc)	$L_{25\,\mu m}$[a] ($L_\odot$)	L_{TIR}[a] ($L_\odot$)	SFR (YSO count) ($M_\odot$ Myr^{-1})	SFR(24 μm) ($M_\odot$ Myr^{-1})	SFR(L_{TIR}) ($M_\odot$ Myr^{-1})	SFR(YSO)/SFR(24 μm)	SFR(YSO)/SFR(L_{TIR})
Cha II	178	14.8	74.7	6.0	0.0724	0.00893	83	670
Lup I	150	6.47	56.0	3.2	0.0349	0.00670	92	480
Lup III	200	11.3	90.7	17.0	0.0569	0.0108	300	1600
Lup IV	150	0.00	2.91	3.0	0.00	0.000348	...	8600
Oph	125	917	6925	72.5	2.79	0.828	26	88
Per	250	715	3796	96.2	2.24	0.454	43	210
Ser	260	41.4	268	56.0	0.180	0.0321	310	1700
Aur N	300	0.00	7.54	0.5	0.00	0.000902	...	550
Aur	300	582	4017	42.8	1.87	0.480	23	89
Cep	300	125	832	29.5	0.479	0.0995	62	300
Cha III	200	10.6	154	1.0	0.0540	0.0185	19	54
Cha I	200	35.2	153	22.2	0.156	0.0184	140	1200
CrA	130	39.8	183	10.2	0.174	0.0219	59	470
IC 5146E	950	1882	16725	23.2	5.28	2.00	4.4	12
IC 5146NW	950	82.5	573	9.5	0.332	0.0685	29	140
Lup VI	150	12.3	78.8	11.2	0.0614	0.00942	180	1200
Lup V	150	15.1	108	10.8	0.0740	0.0129	146	840
Mus	160	1.36	27.4	3.0	0.00879	0.00327	340	920
Sco	130	27.0	184	2.5	0.123	0.0220	20	110
Ser-Aqu	260	2938	20493	360.0	7.83	2.45	46	150

Note. [a] These are luminosities inside extinction contours of $A_V = 2$ ($A_V = 6$ for Serpens and $A_V = 3$ for Ophiuchus) after background subtraction.

clouds are shown in Table 2. For clouds with background emission comparable to the total emission inside the boundaries, namely, Lupus IV and Auriga North, we set the 25 μm luminosities and SFR(24 μm) to zero. With the 25 μm luminosities, the SFR for each cloud was obtained using Equation (2). The differences between luminosities measured at 24 μm and 25 μm should be quite small.

Table 2 compares the SFR(24 μm), which is calculated from the total emission including point sources and diffuse emission, with SFR(YSO count). It is clear from the table that SFR(24 μm) greatly underestimates SFR(YSO count). The average ratio of SFR(YSO count) to SFR(24 μm) is 107 ± 109, with a median of 61.6. Figure 1(a) shows a plot of SFR(24 μm) over SFR(YSO count), and Figure 1(b) shows a ratio of SFR(24 μm)/SFR(YSO count) over SFR(YSO count).

3.3. Contributions from Stellar Continuum Emission

Calzetti et al. (2007) developed relations between SFR and emission at two MIR wavelengths of 8 and 24 μm. Since only the dust emission should measure SFR, stellar continuum emission needed to be subtracted from the flux. The stellar continuum subtraction was performed for the 8 μm emission, but contributions to the 24 μm flux from stars were considered to be negligible. We used c2d clouds as sample regions to see how much stellar continuum contributes to the total flux. The c2d project identified all point sources, which include background and foreground stars, for all clouds. These background/foreground stars in fact dominate the source counts in each cloud. With the available data, we can compare the contributions from point sources, which can be separated into YSO and non-YSO, to the total 24 μm flux. First, we calculated the flux from all identified objects in the 24 μm MIPS images. Then the flux from YSOs was subtracted from the all-object flux to get the non-YSO object flux. In extragalactic studies, when looking at star-forming regions the flux is the total flux emitted from the projected area. To see how much stellar emission contributes to total flux, we compare the non-YSO flux to the total flux (before background subtraction). The results show that stellar continuum contributes very little to the total flux. The contribution is larger for some clouds, specifically clouds with little diffuse emission, but stellar contributions to the total flux are less than 10 percent for all clouds (Table 3).

Table 3
Comparison of Different Sources of 24 μm Emission

Cloud	Total Flux (Jy)	Total Flux after Background Subtraction (Jy)	YSO Flux (Jy)	Non-YSO Object Flux (Jy)
Per	5000	2930	77.1	81.7
Cha II	508	119	7.93	17.9
Oph	18100	15000	94.2	223
Ser	775	157	56.7	47.5
Lup	1406	146	9.45	110

3.4. L_{TIR}

Another tracer of star formation often used in extragalactic studies is the total infrared luminosity. While 24 μm emission arises from warm dust grains or from small, transiently heated dust grains, most of the emission from dust in molecular clouds peaks at a longer wavelength, in the far-infrared. The total infrared luminosity should then trace the bulk of the dust emission. With the available *IRAS* data, the total infrared luminosity (L_{TIR}) for all the c2d and GB clouds can be estimated from

$$L_{TIR} = 0.56 \times D^2 \times (13.48 \times f_{12} + 5.16 \times f_{25} + 2.58 \times f_{60} + f_{100}), \quad (3)$$

where f_i is the flux in each *IRAS* band in units of Jy, D is the distance in kpc, and L_{TIR} (8–1000 μm) is in units of $L_\odot$ (Wu et al. 2010). Each of the *IRAS* bands has a slightly different angular resolution: 3.′8, 3.′8, 4.′0, and 4.′3 for IRIS plate of 12, 25, 60, and 100 μm, respectively (Miville-Deschênes &

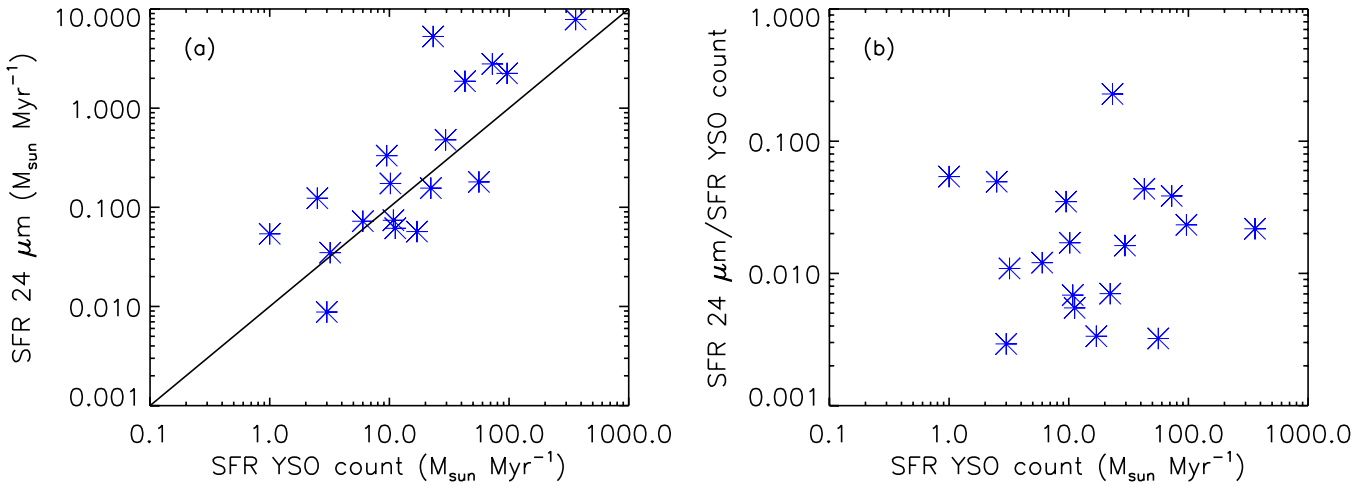

Figure 1. SFR(24 μm) vs. SFR(YSO count) for c2d and Gould Belt clouds, with SFR(24 μm) calculated from the background-subtracted diffuse emission. The solid black line represents a line of SFR(24 μm) = 0.01SFR(YSO count).

(A color version of this figure is available in the online journal.)

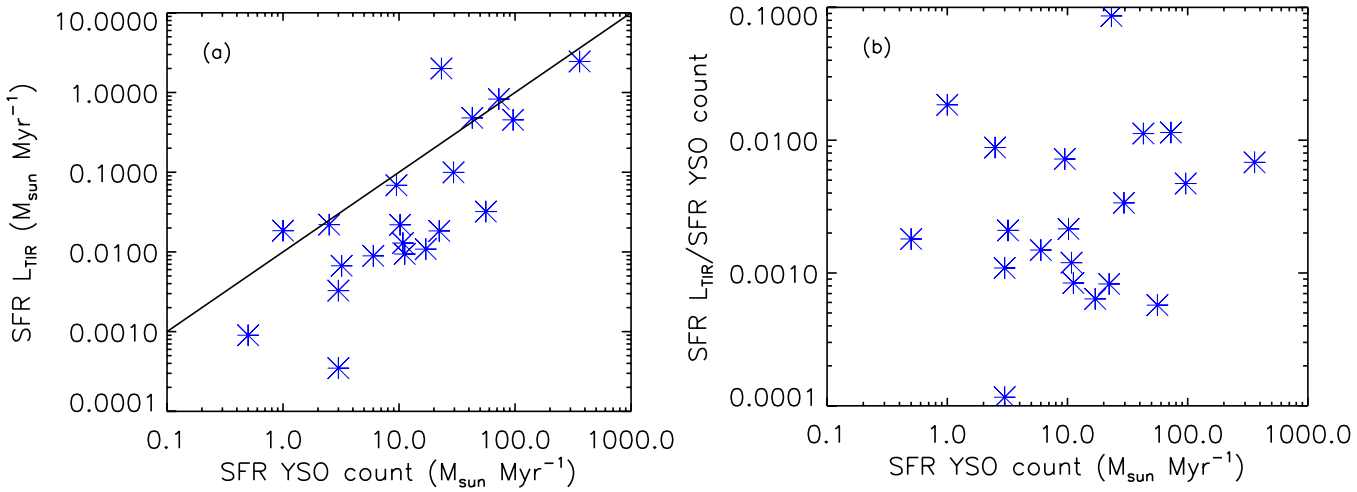

Figure 2. SFR($L_{\rm TIR}$) vs. SFR(YSO count) for c2d and Gould Belt clouds. The solid black line represents the same line as the line in Figure 1 of SFR($L_{\rm TIR}$) = 0.01SFR(YSO count).

(A color version of this figure is available in the online journal.)

Lagache 2005). However, the angular size of our objects is on the order of a few degrees. We therefore did not take into account the differences in the resolutions. The flux in each band was computed with the same technique used for the flux at 25 μm, including background subtraction.

To calculate SFR($L_{\rm TIR}$), we used the extragalactic relation for starburst galaxies from K98. However, the SFR($L_{\rm TIR}$) from K98 assumed a Salpeter form of the IMF. For consistency, all our calculations should be based on the same IMF model. A Salpeter IMF gives a Lyman continuum photon rate of 1.44 times higher than Kroupa IMF (from 0.1 to 100 $M_{\odot}$) for the same SFR (Chomiuk & Povich 2011; Kennicutt et al. 2009). Assuming that $L_{\rm TIR}$ scales with Lyman continuum photon rates, we then divided SFR($L_{\rm TIR}$) from K98 by 1.44 to obtain

$$\mathrm{SFR}(M_{\odot}\ \mathrm{year}^{-1}) = 3.125 \times 10^{-44} L_{\rm TIR}\ (\mathrm{erg\ s}^{-1}), \quad (4)$$

where $L_{\rm TIR}$ is the total infrared luminosity (8–1000 μm).

The results (Table 2) show that $L_{\rm TIR}$ underestimates SFR(YSO count) for all the clouds, with a mean ratio of SFR(YSO count) to SFR($L_{\rm TIR}$) of 969 $\pm$ 1870 and a median of 480. Figure 2(a) shows SFR($L_{\rm TIR}$) over SFR(YSO count), and Figure 2(b) shows the ratio of SFR($L_{\rm TIR}$)/SFR(YSO count) versus SFR(YSO count).

With both the 24 μm and $L_{\rm TIR}$ available, we also compared SFR(24 μm) with SFR($L_{\rm TIR}$). Figure 3 shows SFR(24 μm) over SFR($L_{\rm TIR}$) with the low-mass star-forming cloud data represented by orange circles. The two SFRs agree well with each other with an average ratio of SFR($L_{\rm TIR}$)/SFR(24 μm) of 0.22 $\pm$ 0.08 and a median of 0.33. A curved fit was performed using the MPFITEXY routine (Williams et al. 2010; Markwardt 2009) with adopted uncertainties of 50% for both SFRs. The solid black line represents a line of SFR(24 μm) = SFR($L_{\rm TIR}$), while the dot-dashed, orange line represents a least-squares fit for the nearby clouds of

$$\log[\mathrm{SFR}(24\ \mu\mathrm{m})] = (0.58 \pm 0.13) + (0.91 \pm 0.08) \times \log\ [\mathrm{SFR}(L_{\rm TIR})]. \quad (5)$$

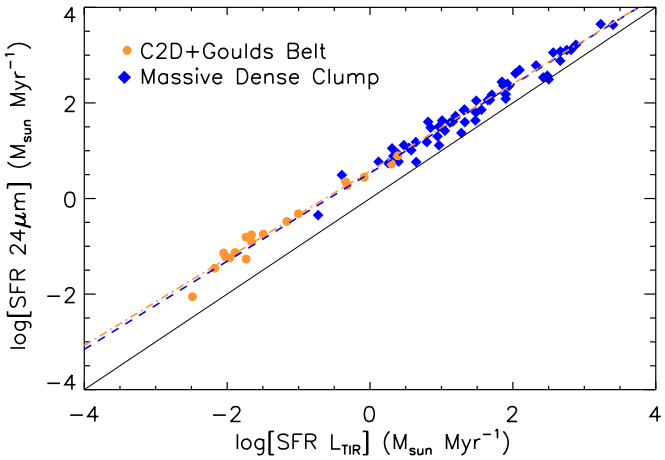

Figure 3. log[SFR(24 μm)] vs. log[SFR($L_{\rm TIR}$)] for c2d, Gould Belt clouds, and massive dense clumps. The solid black line represents a line of SFR(24 μm)/SFR($L_{\rm TIR}$) = 1, a dash-dotted orange line represents a fit to the c2d and Gould Belt cloud data points, and a dotted blue line represents a fit to the massive dense clump data points.

(A color version of this figure is available in the online journal.)

4. ANALYSIS OF REGIONS FORMING HIGH-MASS STARS

So far we have found that the extragalactic relations between SFR and 24 μm or total infrared badly underestimate the SFR in nearby molecular clouds, which are not forming stars of high mass. Here we address the issue for regions forming massive stars, using the dense clump sample discussed in Section 2. These clumps have an average distance of 3.9 ± 2.4 kpc and a median of 3.5 kpc.

4.1. IRAS 25 μm Emission and Total Infrared Luminosity L_{TIR}

The fluxes for the *IRAS* bands for these clumps are available from the *IRAS* point-source catalog (PSC) and tabulated by Mueller et al. (2002). However, most of the massive dense clump sources are extended sources. Examining the images of these sources showed that the *IRAS* PSC could underestimate the flux because the average source size is larger than the *IRAS* beam size. To obtain more accurate values of the flux, we performed photometry on the massive dense clump sample instead of adopting the flux from PSC.

IRAS IRIS images in all four bands were used for photometry. Aperture photometry was performed on each source with the use of IDL routine APER and by setting the aperture radius to be equal to the FWHM of a 1D Gaussian fit. Most of the sources are in a crowded field, which complicated the photometry. Sky subtraction was done by choosing a sky region for each source by eye and averaging the flux within the region to obtain sky level. The result gives a flux in all four *IRAS* bands for a total of 56 sources.

The total infrared luminosity and the SFR($L_{\rm TIR}$) were calculated from the same equation used in the last section (Equations (3) and (4)). Note that $L_{\rm TIR}$ from our photometry is higher than $L_{\rm TIR}$ from the PSC by a factor of two on average. The SFR(24 μm) was also calculated in the same way by using the relation in Equation (2). Ideally, we would now compare the SFRs from infrared emission to SFR(YSO count) as we did for low-mass regions. However, because of the greater distance and the presence of diffuse emission, counting YSOs is not practical in these regions. Without the YSO count, we cannot test the IR SFR tracers against a direct measure of SFR. With more than one method of tracing star formation, we can test to see if different tracers give consistent measures of SFRs.

As shown in Table 4, the two IR SFRs are comparable to each other with the average ratio of SFR($L_{\rm TIR}$)/SFR(24 μm) = 0.41 ± 0.19. The median is 0.37. Figure 3 shows the comparison between SFR(24 μm) and SFR($L_{\rm TIR}$) for the clumps, which is represented by blue diamonds. The dashed blue line represents a least-squares fit for the massive dense clump data of

$$\log[\mathrm{SFR}(24\ \mu\mathrm{m})] = (0.53 \pm 0.08) + (0.92 \pm 0.05) \times \log[\mathrm{SFR}(L_{\rm TIR})]. \quad (6)$$

4.2. Radio Continuum Emission

In addition to infrared emission, radio continuum emission is also used as an SFR tracer for galaxies in several studies (Condon 1992; Yun et al. 2001; Jogee et al. 2005; Murphy et al. 2011). For normal and starburst galaxies, most of the radio emission is free–free emission from ionized gas and synchrotron emission from relativistic electrons (Yun et al. 2001). Free–free emission traces ionized gas inside H II regions, along with some more diffuse emission from extended ionized gas, while synchrotron emission traces relativistic electrons accelerated by supernova remnants, which are much more widely distributed. Both of the sources of the radio emission are related to high-mass star formation because high-mass stars produce H II regions while stars with $M \geqslant 8\,M_{\odot}$ produce core-collapse supernovae (Yun et al. 2001). However, the quantitative relation between synchrotron emission and star formation is less direct, being derived from a correlation between the synchrotron and far-infrared emission (de Jong et al. 1985; Helou et al. 1985; Condon 1992).

For this study, we used radio continuum as another independent source of SFR tracer for comparison with $L_{\rm TIR}$ since both radio continuum and $L_{\rm TIR}$ should trace the presence of high-mass stars. In a spectrum of a whole galaxy, synchrotron emission dominates emission at $\nu \leqslant 30$ GHz (Condon 1992). However, our samples are on much smaller scales than for extragalactic studies. In the absence of nearby supernova remnants, radio emission from high-mass star-forming regions is dominated by thermal free–free emission. To use radio continuum as an SFR tracer for the massive dense clump samples, we need to connect free–free emission to a total number of massive stars. Thermal (free–free) luminosity is related to the rate of photoionizing photons (Lyman continuum photons) by

$$\left(\frac{N_{\rm UV}}{\mathrm{phot\ s^{-1}}}\right) > 6.3 \times 10^{52} \left(\frac{T_e}{10^4\ \mathrm{K}}\right)^{-0.45} \left(\frac{\nu}{\mathrm{GHz}}\right)^{0.1} \times \left(\frac{L_T}{10^{20}\ \mathrm{W\ Hz^{-1}}}\right), \quad (7)$$

where $N_{\rm UV}$ is the production rate of Lyman continuum photons per second, T_e is the electron temperature, ν is the frequency, and L_T is the thermal emission luminosity, assuming that it is optically thin in this part of the spectrum (Condon 1992). Using Kroupa's IMF and the stellar spectral model from Starburst99 (Leitherer et al. 1999), the rate of photoionizing photons is related to SFR by (Chomiuk & Povich 2011)

$$\frac{\mathrm{SFR}}{M_{\odot}\ \mathrm{yr^{-1}}} = 7.5 \times 10^{-54} \left(\frac{N_{\rm UV}}{\mathrm{phot\ s^{-1}}}\right). \quad (8)$$

Table 4
Massive Dense Clump Sample

Object	Distance (kpc)	$\log(L_{25\,\mu m})$ ($L_\odot$)	$\log(L_{TIR})$ ($L_\odot$)	SFR(24 μm) ($M_\odot$ Myr^{-1})	SFR(L_{TIR}) ($M_\odot$ Myr^{-1})	SFR(L_{TIR})/SFR(24 μm)
G121.30+0.66	1.2	2.07	3.20	0.4	0.2	0.42
G123.07−6.31	2.2	3.66	4.47	11.5	3.5	0.30
W3(2)	2.4	5.50	6.02	490.0	124.0	0.25
W3(OH)	2.4	4.49	5.40	62.7	30.3	0.48
GL490	0.9	3.01	3.53	3.1	0.4	0.13
S231	2.3	3.33	4.04	5.9	1.3	0.22
S235	1.6	3.72	4.40	13.0	3.0	0.23
S241	4.7	3.79	4.72	15.2	6.2	0.41
MonR2	0.9	4.27	4.74	40.3	6.5	0.16
S252A	1.5	3.29	4.18	5.5	1.8	0.33
S255	1.3	3.79	4.56	15.2	4.4	0.29
RCW142	2.0	4.26	5.04	38.9	13.2	0.34
W28A2(1)	2.6	5.17	5.85	251.9	83.7	0.33
M8E	1.8	4.30	4.93	42.9	10.2	0.24
G9.62+0.10	7.0	4.92	5.82	152.2	79.4	0.52
G8.67−0.36	4.5	4.06	4.97	26.2	11.2	0.43
W31(1)	12.0	5.28	6.42	311.6	317.8	1.02
G10.60−0.40	6.5	5.32	6.35	341.4	265.7	0.78
G12.42+0.50	2.1	3.64	4.23	11.2	2.0	0.18
G12.89+0.49	3.5	3.72	4.89	13.0	9.2	0.71
G12.21−0.10	13.7	5.36	6.40	371.6	302.4	0.81
G13.87+0.28	4.4	4.77	5.41	111.3	30.7	0.28
W33A	4.5	4.79	5.57	115.1	44.4	0.39
G14.33−0.64	2.6	3.32	4.57	5.8	4.4	0.76
G19.61−0.23	4.0	4.79	5.60	115.4	47.7	0.41
G20.08−0.13	3.4	3.93	4.87	20.0	8.8	0.44
G23.95+0.16	5.8	4.91	5.63	148.7	50.8	0.34
G24.49−0.04	3.5	4.26	5.25	39.6	21.3	0.54
W42	9.1	5.97	6.74	1287.2	652.6	0.51
G28.86+0.07	8.5	4.82	5.82	122.5	79.3	0.65
W43S	8.5	6.09	6.80	1649.3	760.7	0.46
G31.41+0.31	7.9	4.30	5.40	43.0	29.8	0.69
G31.44−0.26	10.7	5.13	5.79	231.3	73.5	0.32
W44	3.7	5.12	5.87	226.6	88.3	0.39
S76E	2.1	4.41	5.12	53.1	15.7	0.30
G35.58−0.03	3.5	4.56	5.48	72.0	36.3	0.50
G35.20−0.74	3.3	4.28	5.08	40.9	14.5	0.35
W49	14.0	6.56	7.33	4301.0	2530.4	0.59
OH43.80−0.13	2.7	3.60	4.50	10.2	3.8	0.37
G45.07+0.13	9.7	5.91	6.49	1133.5	366.5	0.32
G48.61+0.02	11.8	5.72	6.58	764.1	459.9	0.60
W51W	7.0	5.97	6.68	1280.4	567.7	0.44
W51M	7.0	6.58	7.15	4461.3	1695.4	0.38
G59.78+0.06	2.2	3.52	4.31	8.7	2.4	0.28
S87	1.9	4.13	4.77	30.4	7.0	0.23
S88B	2.1	4.54	5.24	69.9	20.6	0.29
K3−50	9.0	5.94	6.59	1196.5	463.2	0.39
ON1	6.0	4.01	5.20	23.6	19.0	0.81
ON2	5.5	5.61	6.25	610.2	211.0	0.35
S106	4.1	5.42	5.96	415.6	108.6	0.26
G97.53+3.19	7.9	4.56	5.24	72.8	21.0	0.29
BFS11-B	2.0	3.46	4.25	7.7	2.1	0.28
CepA	0.7	3.33	4.32	5.9	2.5	0.42
S158	2.8	5.22	5.77	275.8	70.1	0.25
NGC 7538-IRS9	2.8	5.21	5.77	272.8	70.8	0.26
S157	2.5	4.16	4.89	31.8	9.2	0.29

We get

$$\frac{\mathrm{SFR}}{M_\odot\ \mathrm{yr}^{-1}} = 0.47\left(\frac{T_e}{10^4\ \mathrm{K}}\right)^{-0.45}\left(\frac{\nu}{\mathrm{GHz}}\right)^{0.1}\left(\frac{L_T}{10^{20}\ \mathrm{W\ Hz}^{-1}}\right).$$

For an electron temperature of $T_e \sim 10^4$ K, the thermal radio SFR relation is

$$\frac{\mathrm{SFR}}{M_\odot\ \mathrm{yr}^{-1}} = 0.47\times10^{-20}\left(\frac{\nu}{\mathrm{GHz}}\right)^{0.1}\left(\frac{L_T}{\mathrm{WHz}^{-1}}\right). \quad (9)$$

Table 5
Massive Dense Clump/Radio Continuum Sample

Object	Distance (kpc)	Radio Frequency (GHz)	FWHM (arcmin)	Radio Flux[a] (Jy)	$\log(L_{\rm TIR})$[b] ($L_\odot$)	SFR(radio) ($M_\odot$ Myr^{-1})	SFR($L_{\rm TIR}$) ($M_\odot$ Myr^{-1})	SFR(radio)/SFR($L_{\rm TIR}$)
W28A2(1)	2.6	4.875	4.0	5.5	5.71	58.0	62.0	0.94
G9.62+0.19	7.0	"	2.8	1.12	5.66	41.9	54.1	0.77
W31(1)	12.0	"	3.1	1.11	6.21	150	196	0.77
G10.60−0.40	6.5	"	3.2	4.46	6.14	188	167	1.1
G12.21−0.10	13.7	"	3.3	1.67	6.23	333	205	1.6
G13.87+0.28	4.4	"	2.7	3.83	5.31	52.7	24.3	2.2
G19.61−0.23	4.0	"	2.9	4.98	5.33	65.3	25.7	2.5
G20.08−0.13	3.4	"	3.0	1.13	4.61	11.5	4.83	2.4
G23.95+0.16	5.8	"	2.7	2.32	5.38	55.5	28.4	2.0
G24.49−0.04	3.5	"	3.1	0.62	4.64	7.12	5.26	1.4
W43S	8.5	"	5.0	4.5	6.64	792	527	1.5
G31.41+0.31	7.9	"	2.6	1.2	5.04	49.4	12.6	3.7
G31.44−0.26	10.7	"	3.4	1.06	5.77	137	70.6	1.9
W44	3.7	"	2.8	11.58	5.73	121	64.9	1.9
G35.58−0.03	3.5	"	3.6	1.68	5.06	26.0	13.6	1.9
G48.61+0.02	11.8	"	3.9	3.51	6.40	725	303	2.4
W51W	7.0	"	3.5	13.5	6.43	790	325	2.4
W51M	7.0	"	3.5	58	6.82	3390	783	4.3
S76E	2.1	5.000	9.5	7	5.20	20.4	18.9	1.1
S87	1.9	2.695	9.0	2	4.86	4.48	8.67	0.52
S88B	2.1	"	7.0	9	5.30	24.7	23.7	1.0
K3−50	9.0	"	8.5	23	6.67	1160	558	2.1

Notes.
[a] This column gives a peak flux for 4.875 GHz data from A79 and an integrated flux for the last four objects from A70.
[b] $L_{\rm TIR}$ data obtained from photometry of *IRAS* images with aperture radius = FWHM.

For the radio continuum data, we used radio surveys that cover the regions of the Galactic plane that coincide with the massive dense clump sample. The radio data in this study were obtained from two surveys. The first set of data came from a survey of the Galactic plane at 4.875 GHz by Altenhoff et al. (1979, hereafter A79). The radio data were obtained with the 100 m Effelsberg with a half-power beamwidth of 2.′6 over the galactic longitude range of $l = 357.^\circ5$ to 60° and galactic latitude of $b = \pm 2^\circ$. The second set of radio data were obtained from an earlier survey by Altenhoff et al. (1970, hereafter A70). The survey of the Galactic plane at 1.414, 2.695, and 5.000 GHz covered a range of $l = 335^\circ$ to 75° and $b = \pm 4^\circ$ with a half-power beamwidth of approximately 11′. The observations for the three wavelength bands were made with the 300 foot transit paraboloid antenna at the NRAO, the 140 foot antenna at NRAO, and the 85 foot parabolic antenna at Fort Davis for 1.414, 2.695, and 5.000 GHz, respectively (Altenhoff et al. 1970). Using the 4.875 GHz (A79) survey has the advantage of having a comparable resolution to the infrared data from *IRAS* (2.′6 for A79 and ∼2′ for *IRAS* 100 μm), making it suitable for comparison between radio and infrared data.

We first matched objects from the radio surveys to the massive dense clump objects by matching their coordinates. The matching objects have center coordinates within a few arcminutes of each other. Lockman (1989) provides radio recombination line data for these radio sources from his survey of radio H II regions in the northern sky. We compared radio recombination line velocities of matched objects to line velocities (HCN $J = 1 \rightarrow 0$, $J = 3 \rightarrow 2$ and CS $J = 2 \rightarrow 1$, $J = 7 \rightarrow 6$) from Wu et al. (2010). We kept the objects with velocities approximately within ± 5 km s^{-1} between the two data sets. Our matching resulted in a total of 22 objects with available radio continuum flux, radio recombination line velocity, and infrared luminosity.

A79 provides a peak intensity for each radio source along with an FHWM. The integrated flux for each object was calculated for a total of 18 objects by assuming a Gaussian profile for both the source flux distribution and the beam profile. A70 provides integrated flux and FWHM data for an additional 4 objects. Then SFR(radio) was calculated from Equation (7). After obtaining SFR(radio), our next step was to compare them to IR SFR. However, in order to compare radio data to infrared data, the two sets of data should come from equal areas of the objects. Aperture photometry was performed on *IRAS* IRIS images with a chosen aperture radius equal to the radio FWHM size of each object. The aperture size was chosen to capture most of the infrared flux of the objects without contamination from other nearby sources and to make the observed areas comparable to those of the radio data.

The resulting SFR(radio), $L_{\rm TIR}$, SFR($L_{\rm TIR}$) and SFR(24 μm) are included in Table 5. SFR(radio) and SFR($L_{\rm TIR}$) are well correlated, with an average ratio of SFR(radio)/SFR($L_{\rm TIR}$) of 1.8 ± 0.8, a median of 1.9, and a linear correlation coefficient of 0.90. There are many sources of uncertainties in our calculations of SFR, which makes it difficult to estimate realistic errors for each source. We instead adopted 50% uncertainties for both SFRs and performed a curve fit using the MPFITEXY routine (Williams et al. 2010; Markwardt 2009). Figure 4(a) shows SFR($L_{\rm TIR}$) versus SFR(radio) with a solid line representing SFR ratio of 1 and a dashed line representing a best fit to the data of

$$\log\,[\mathrm{SFR}(L_{\rm TIR})] = (0.0029 \pm 0.18) + (0.89 \pm 0.085) \times \log[\mathrm{SFR(radio)}]. \quad (10)$$

SFR(radio) and SFR(24 μm) are also well correlated with an average ratio of SFR(radio)/SFR(24 μm) of 0.76 ± 0.42, a median of 0.79, and a linear correlation coefficient of 0.98.

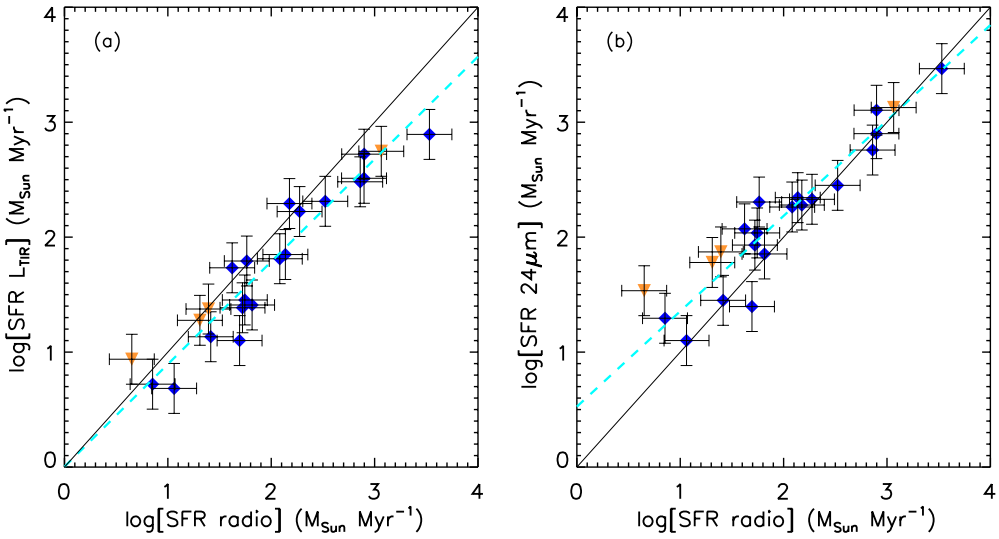

Figure 4. SFR(L_{TIR}) vs. SFR(radio) for massive dense clumps. The blue squares represent data from A79, and the orange triangles represent data from A70. The solid black line represents a line where the two SFRs are equal, while the blue dashed line represents a fit of log[SFR(L_{TIR})] = 0.0029 + 0.89 log[SFR(radio)].

(A color version of this figure is available in the online journal.)

Figure 4(b) shows SFR(24 μm) versus SFR(radio) with a dashed line representing a best fit of

$$\log[\mathrm{SFR}(24\ \mu\mathrm{m})] = (0.53 \pm 0.17) + (0.83 \pm 0.08) \times \log[\mathrm{SFR(radio)}]. \quad (11)$$

5. DISCUSSION

5.1. Low-mass SF

From the results for the c2d and Gould Belt survey, it is clear that the SFRs from 24 μm do not agree well with SFRs from YSO counting. First of all, 24 μm emission from YSO point sources contributes very little to the total emission of the clouds. Even when we included the diffuse emission in our calculation of SFR(24 μm), the resulting values are still much lower (by a factor of about 100 than SFR(YSO count)). Nonetheless, we can ask whether there is any relation at all between SFR(24 μm) and SFR(YSO count). Figure 1(a) shows a plot of SFR(24 μm) versus SFR(YSO count). The solid black line represents a ratio of 100. The figure shows that there is a general correlation between the two with the Pearson linear correlation coefficient of 0.83. Perhaps the 24 μm emission might provide a rough guide to the SFR, but with a different conversion factor. However, the scatter is large. Figure 1(b) shows the ratio of SFR(24,diffuse)/SFR(YSO count). The discrepancies and scatter between the two SFRs persist throughout the range of SFRs. A similar result was obtained for the comparison of SFR(L_{TIR}) with SFR(YSO count), as shown in Figure 2. There is again a weak correlation with a correlation coefficient of 0.77, but the underestimate of SFR(YSO count) is even greater. The solid black line represents the same line of SFR(YSO count) = 100 × SFR(L_{TIR}), as shown in Figure 2(a).

The disagreement between SFR(IR) and SFR(YSO count) is not surprising since these clouds are not forming very massive stars, which would dominate the luminosity if the IMF is fully sampled. The undersampling of the IMF, along with other possible causes behind the discrepancy in SFRs, is discussed below.

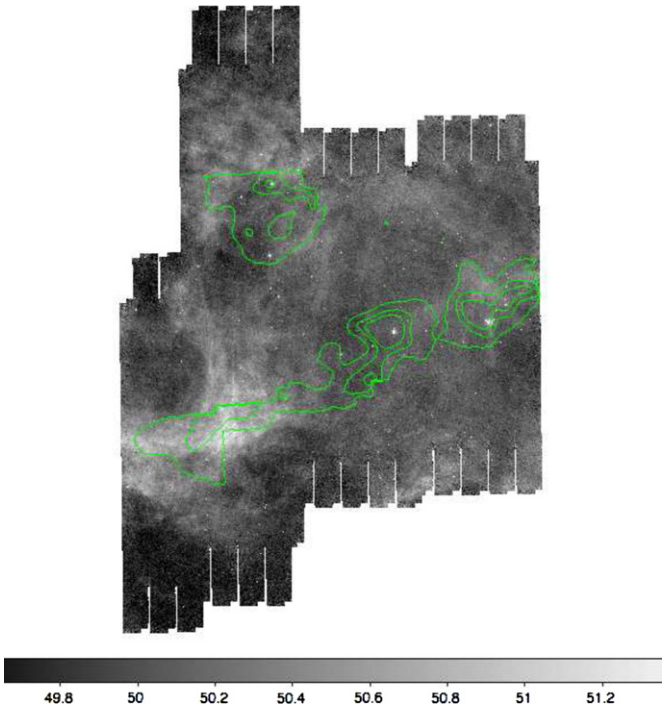

Figure 5. MIPS 24 μm image of the Lupus I cloud with contours of A_V = 2, 4, and 6 mag in green.

(A color version of this figure is available in the online journal.)

5.1.1. External Heating

As discussed earlier, the total fluxes from the actual clouds are generally small fractions of the total emission toward the regions, which means that a lot of the emission is background emission. Furthermore, much of the diffuse emission that is associated with the cloud does not correspond to regions of high extinction or intense ongoing star formation. As examples, Figures 5 and 6 show the images for Lupus I and Ophiuchus, with extinction contour levels overlaid. In Lupus I, the diffuse emission at 24 μm is located away from the regions of current star formation. In contrast, in Ophiuchus, most of the diffuse

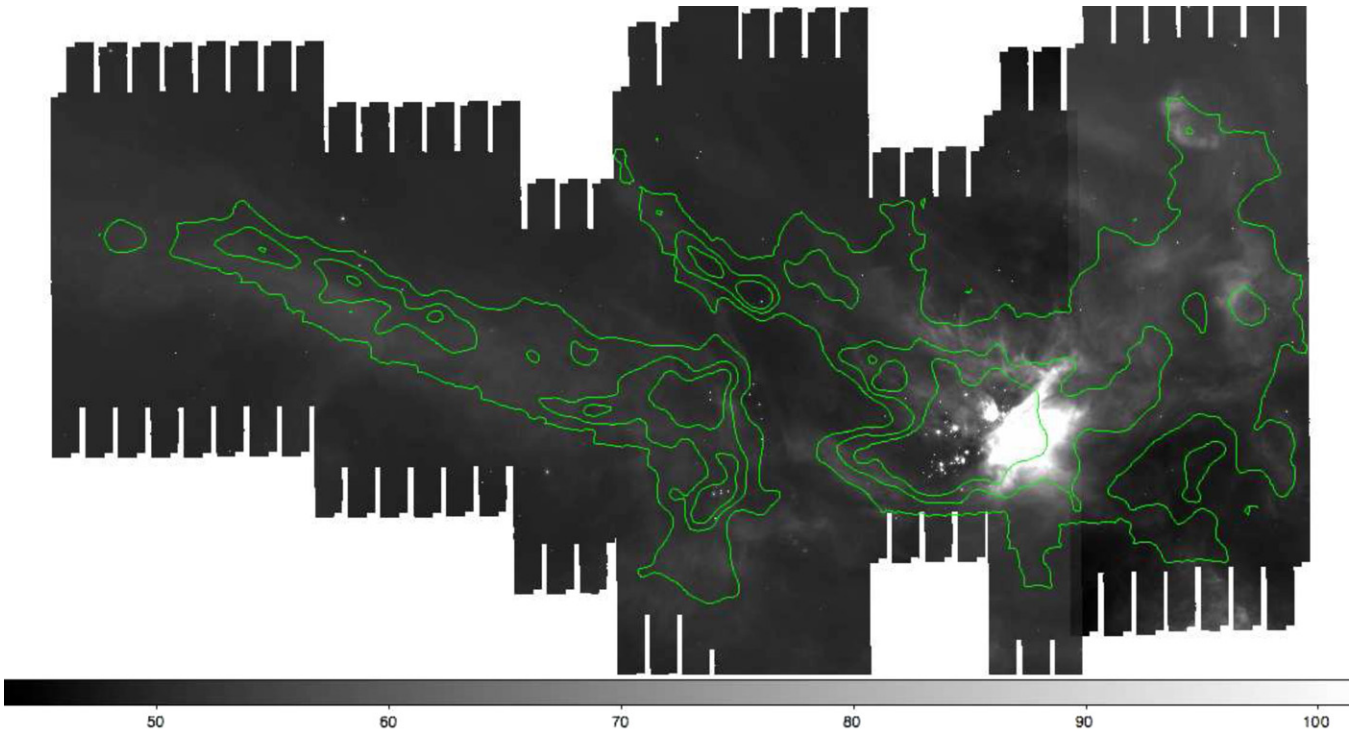

Figure 6. MIPS 24 μm image of the Ophiuchus cloud with contours of $A_V = 2$, 6, and 10 mag in green.
(A color version of this figure is available in the online journal.)

emission is associated with the cluster of forming stars spatially, and the excitation peaks on embedded early-type stars (Padgett et al. 2008, see Figure 2). In the case of the Perseus cloud, much of the diffuse 24 μm emission comes from regions heated by a star lying behind the cloud (unrelated to current star formation) or from the IC 348 cluster (related to recent star formation) (Rebull et al. 2007). Such differences from cloud to cloud will introduce large scatter into the relations. In the absence of high-mass stars in these clouds, external sources of heating could dominate the infrared emission.

The *IRAS* 100 μm images show more correlation with the extinction contours than the 25 μm images. The contribution to the $L_{\rm TIR}$ is also larger from the 100 μm, which is closer to the peak of the general dust emission from molecular clouds. The resulting $L_{\rm TIR}$ may then trace the amount of dust inside the clouds as opposed to star formation in the clouds. Then the correlation in Figure 2 could be a secondary effect of the correlation of SFR with amount of dust for the cloud as a whole.

5.1.2. Undersampled IMF

Since these clouds are not forming very massive stars, clearly there are no stars to populate the high end of the IMF. The lack of high-mass stars means that it requires more mass in the form of lower-mass stars to produce a certain luminosity than if the IMF is fully sampled. Using SFR relations derived by assuming the full IMF will then underestimate the SFR in these regions.

To see how much this affects the discrepancies in the SFRs, we looked at the details of the SFR calibrations. Calzetti et al. (2007) calibrated the SFR–24 μm relation by empirically fitting $L(24\,\mu{\rm m})$ to Hα. Hα was then connected to SFR through a stellar population model assuming Kroupa's IMF, solar metallicity, and a constant SFR over a timescale of 100 Myr. Any differences in the IMF would have an effect on the two steps: SFR–Hα (or directly related, $N_{\rm UV}$) relation and Hα/24 μm ratio. We performed a test by running Starburst99 with the same IMF but with a different upper limit on the stellar mass ($M_{\rm upper}$). We also assume that a constant fraction of the bolometric luminosity ($L_{\rm bol}$) is being re-emitted in the 24 μm band.

Taking the Perseus molecular cloud as an example, the highest-mass star in the cloud is an early B star (Rebull et al. 2007). We set $M_{\rm upper} = 15\,M_\odot$ and a constant SFR over 100 Myr. The results showed an underestimation of SFR(24 μm) by a factor of 2.1 when assuming a full IMF. For SFR($L_{\rm TIR}$), the relation in Equation (4) was derived from assuming that all of $L_{\rm bol}$ is re-emitted in the infrared so that $L_{\rm bol} = L_{\rm TIR}$. $L_{\rm bol}$ was connected to SFR directly from the stellar synthesis model. This would result in the same underestimation of SFR($L_{\rm TIR}$) by a factor of 2.1.

A factor of two difference from the cutoff IMF is still much less than the observed discrepancies in SFR(YSO count)/SFR(24 μm) of a factor of 43 and SFR(YSO count)/SFR($L_{\rm TIR}$) of 210 in Perseus. The effect of undersampling the IMF on underestimating the SFR will be greater for clouds with lower $M_{\rm upper}$. For many clouds $M_{\rm upper}$ is even lower than $15\,M_\odot$. We tested the model with $M_{\rm upper} = 5\,M_\odot$, which showed an underestimation of SFR by a factor of 10. Even with the lower $M_{\rm upper}$, undersampled IMF still cannot account for the large discrepancies in the whole sample. We tested the effect of undersampling IMF by changing $M_{\rm upper}$, but in regions of low SFR stochastic sampling of the IMF could also be important, especially in contributing to the scatter in the sample (da Silva et al. 2012; Eldridge 2012).

5.1.3. Star Formation Timescale

The timescale of constant star formation assumed in the SFR relations is 100 Myr, much longer than a lifetime of an average molecular cloud (few $\times 10^7$ yr; McKee & Ostriker 2007; Murray 2011) or the timescale over which YSO counting is relevant

(≈5 Myr). On a longer timescale the contribution of high-mass stars to the total luminosity will get smaller since low-mass stars will outlast the short-lived high-mass stars. On the timescale of molecular clouds, not accounting for the lack of massive stars will lead to even greater underestimations of SFR than on a longer timescale. Taking an average age of the clouds to be 10 Myr, the model results from combining the cutoff IMF ($M_{\rm upper} = 15\,M_{\odot}$) and the change in timescale showed a higher SFR by a factor of 9.9, still lower than the observed differences in Perseus. Combining the change in timescale to 10 Myr and a cutoff IMF of $M_{\rm upper} = 5\,M_{\odot}$ gave a higher SFR by a factor of 110, close to the average discrepancy in our data.

Additionally, the assumption that all of the bolometric luminosity is being re-emitted in the infrared might not be valid in these regions. If the fraction of energy emitted in the infrared or 24 μm band over $L_{\rm bol}$ is not constant or is lower in regions with low SFR than in the regions used in the SFR calibration, then this would be another cause for underestimation of the SFR.

5.2. High-mass SF

5.2.1. L_{TIR} and 24 μm

Limited resolution, extinction, and the confusing effects of diffuse emission prevent accurate star counts for the massive dense clumps. Instead, we calculated the SFR from both 25 μm and total infrared emission. There is a good correlation between SFR(24 μm) and SFR($L_{\rm TIR}$). Ideally, this would mean that both 24 μm and $L_{\rm TIR}$ can trace SFR well in high-mass star-forming regions. However, without an absolute SFR for comparison, we cannot tell if the SFRs from both tracers are accurate or if the calibration is off by some factor. Moreover, the correlation could also result if all the clumps have similar SEDs.

One way to distinguish these explanations is to compare SFR(24 μm) and SFR($L_{\rm TIR}$) in low-mass star-forming clouds. If they show a strong correlation even when both fail to represent an accurate SFR, the explanation of similar SEDs is likely. SFR(24 μm) is plotted versus SFR($L_{\rm TIR}$) for both the massive dense clump sample and the nearby cloud sample in Figure 3. The solid black line represents a line of SFR(24 μm)/SFR($L_{\rm TIR}$) = 1. For both data sets, SFR(24 μm) is higher than SFR($L_{\rm TIR}$) on average with the average ratio of SFR(24 μm)/SFR($L_{\rm TIR}$) higher for the nearby cloud sample than for the high-mass sample. The dashed red line represents a fit for the nearby clouds, while the dash-dotted green line represents a fit for the massive dense clump data. The fact that both fit similar relationships, even though we know that neither SFR($L_{\rm TIR}$) nor SFR(24 μm) is accurately tracing SFR in the nearby clouds, suggests that the correlation is mostly driven by the similarity of the SEDs.

The nearby cloud sample shows a smaller scatter in the data than the high-mass sample. The smaller scatter in the low-mass sample suggests that the SEDs for low-mass star-forming clouds are more uniform than those of massive dense clumps. If the diffuse dust continuum emission is dominated by grains responding to the general interstellar radiation field, the SED would be fairly uniform. In regions forming massive stars, the dust energetics could instead be dominated by luminous sources internal to the cloud, and the SED would depend more on the distribution of luminosities of the sources and the geometry.

5.2.2. IR and Radio Continuum

After comparing SFR(24 μm) to SFR($L_{\rm TIR}$), we then compared them to SFR(radio). The thermal radio emission comes from a different mechanism than the infrared emission. While infrared emission mostly traces dust surrounding H II regions, thermal radio traces ionized gas inside H II regions. Radio data then provide a more independent tracer of SFR in a different part of the spectrum. The result shows that SFR(radio) also correlates very well with $L_{\rm TIR}$ with a correlation coefficient of 0.90. Radio data give a slightly larger SFR than does $L_{\rm TIR}$, as shown in Figure 4(a), where a solid line represents an SFR ratio of 1 and the dashed line represents a best fit. Similarly, 24 μm also correlates well with radio data as shown in Figure 4(b). In the area of 24 μm the SFR(radio) is slightly lower than SFR(24 μm) on average. The fact that SFR(radio) and SFR($L_{\rm TIR}$) are comparable to each other could indicate that both radio emission and infrared emission originate from the same source of heating, namely, photons from high-mass stars.

The radio and infrared data also imply a good correlation between $L_{\rm TIR}$ and radio luminosity. As seen from many previous studies, FIR-radio correlations have been well observed among galaxies with a wide luminosity range and spatial scales (Murphy et al. 2006; Dumas et al. 2011; Hughes et al. 2006; Tabatabaei et al. 2007; Zhang et al. 2010). It is interesting that even though radio continuum emission in galaxies is dominated by synchrotron emission instead of free–free emission, our results still show that the correlation between TIR and radio emission extends down to parsec scales in high-mass star-forming regions.

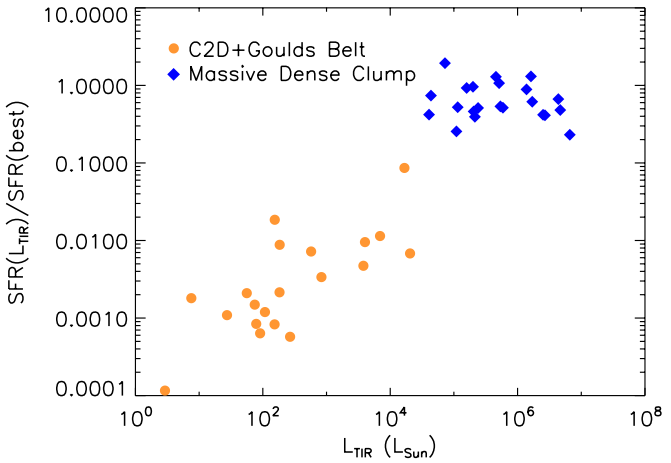

Figure 7. SFR($L_{\rm TIR}$)/SFR(best) vs. $L_{\rm TIR}$, where SFR(best) refers to SFR(YSO count) for low-mass regions and SFR(radio) for high-mass regions. Blue stars represent low-mass clouds (c2d+GB), and orange stars represent high-mass regions (massive dense clump).

(A color version of this figure is available in the online journal.)

5.3. Combining Both Samples

Our results indicate that $L_{\rm TIR}$ underestimates SFR by a large factor for low-mass regions while $L_{\rm TIR}$ gives consistent (within a factor of two) SFR with SFR(radio) for high-mass regions. Figure 7 shows the ratio of SFR($L_{\rm TIR}$)/SFR(best) for both low-mass and high-mass regions. SFR(best) refers to SFR(YSO count) for low-mass regions and SFR(radio) for high-mass regions. We note that SFR(YSO count) is a more direct measurement of current SFR than SFR(radio), which depends on certain assumptions that went into the calibration. With the lack of SFR(YSO count) for high-mass regions, we use SFR(radio) as a comparison. The blue stars, which represent low-mass clouds, show a general trend between the SFR ratio and $L_{\rm TIR}$. SFR($L_{\rm TIR}$)

is closer to the SFR(YSO count) at higher $L_{\rm TIR}$. $L_{\rm TIR}$ traces SFR better for $L_{\rm TIR}$ closer to $\approx 10^{4.5}$ $L_{\odot}$, which is a transition between regions forming low-mass and regions forming high-mass stars. If SFR(radio) gives an accurate measure of SFR, then the results would mean that SFR($L_{\rm TIR}$) is a good tracer above $10^{4.5}$ $L_{\odot}$. This result would be consistent with the suggestion by Wu et al. (2005b) that the $L_{\rm TIR}$ traces star formation above that luminosity. Resolving YSOs in regions forming high-mass stars is a next important step in further understanding of the use of these tracers.

The failure of SFR(24 μm) and SFR($L_{\rm TIR}$) to accurately trace SFR in nearly all the nearby clouds has some interesting implications. An observer in another galaxy using Hα or radio continuum emission would miss all star formation in a 300 pc radius of the Sun; we find that using 24 μm emission would underestimate the local star formation by a factor of about 100. If the local volume were representative of most star formation in galaxies, the SFRs would be vastly underestimated. The fact that the same extragalactic observers would get the *global* SFR in the Milky Way right to a factor of about two (Chomiuk & Povich 2011) indicates that most star formation in the Milky Way occurs in regions forming massive stars, but this might not be the case in the outer parts of the galaxies.

Finally, we note that the apparently good correlation of two purported tracers of star formation, even in regimes where neither is accurate, serves as a warning about accepting "consistency" as evidence of accuracy.

6. SUMMARY

We studied two groups of star-forming clouds in the Milky Way: 20 nearby clouds from *Spitzer* c2d and Gould Belt Legacy surveys, and 32 massive dense clumps that are forming massive stars. We determined the total diffuse 24 μm emission for each cloud and calculated the corresponding SFR using the relation from Calzetti et al. (2007). Comparing 24 μm images with extinction maps shows that a significant portion of 24 μm emission does not come from star-forming regions in some clouds. We calculated the total infrared emission from the *IRAS* data and the corresponding SFR. For massive dense clumps, we also obtained radio continuum data and calculated SFR(radio) for a total of 22 clumps. Then the resulting SFRs were compared with SFRs calculated using the method of counting number of YSOs for the nearby clouds. We compared SFR($L_{\rm TIR}$) with SFR(24 μm) and SFR(radio) for massive dense clumps. The comparison shows quite a good correlation between the three SFR tracers for the massive dense clumps, which are high-mass star-forming regions, with the average ratio of SFR($L_{\rm TIR}$)/SFR(24 μm) $= 0.6 \pm 0.6$ and SFR(radio)/SFR($L_{\rm TIR}$) $= 1.8 \pm 0.9$.

Neither SFR(24 μm) nor SFR($L_{\rm TIR}$) traces the SFR(YSO count) accurately in the nearby clouds, where we can calibrate with an independent method. There is a weak correlation between both tracers and SFR(YSO count), but a very different calibration value would be needed, and the scatter is large. Both 24 μm and $L_{\rm TIR}$ severely underestimate SFR for the nearby clouds. SFR($L_{\rm TIR}$) shows better agreement to SFR(YSO count) for clouds with higher luminosity.

We thank G. Helou for suggesting this study and the referee for suggestions that improved the work. We also thank Mike Dunham and Amanda Heiderman for helpful discussions. We acknowledge support from NSF Grant AST-1109116 to the University of Texas at Austin.

REFERENCES

Alonso-Herrero, A., Rieke, G. H., Rieke, M. J., et al. 2006, ApJ, 650, 835
Altenhoff, W. J., Downes, D., Goad, L., Maxwell, A., & Rinehart, R. 1970, A&AS, 1, 319
Altenhoff, W. J., Downes, D., Pauls, T., & Schraml, J. 1979, A&AS, 35, 23
Bigiel, F., Leroy, A., Walter, F., et al. 2008, AJ, 136, 2846
Buat, V., Iglesias-Páramo, J., Seibert, M., et al. 2005, ApJL, 619, L51
Burgarella, D., Buat, V., & Iglesias-Páramo, J. 2005, MNRAS, 360, 1413
Calzetti, D., Kennicutt, R. C., Engelbracht, C. W., et al. 2007, ApJ, 666, 870
Calzetti, D., Kinney, A. L., & Storchi-Bergmann, T. 1994, ApJ, 429, 582
Calzetti, D., Wu, S.-Y., Hong, S., et al. 2010, ApJ, 714, 1256
Carey, S. J., Noriega-Crespo, A., Mizuno, D. R., et al. 2009, PASP, 121, 76
Chabrier, G. 2003, PASP, 115, 763
Chomiuk, L., & Povich, M. S. 2011, AJ, 142, 197
Condon, J. J. 1992, ARA&A, 30, 575
da Silva, R. L., Fumagalli, M., & Krumholz, M. 2012, ApJ, 745, 145
de Jong, T., Klein, U., Wielebinski, R., & Wunderlich, E. 1985, A&A, 147, L6
Draine, B. T., Dale, D. A., Bendo, G., et al. 2007, ApJ, 663, 866
Dumas, G., Schinnerer, E., Tabatabaei, F. S., et al. 2011, AJ, 141, 41
Eldridge, J. J. 2012, MNRAS, 422, 794
Evans, N. J., II, Allen, L. E., Blake, G. A., et al. 2003, PASP, 115, 965
Evans, N. J., II, Dunham, M. M., Jørgensen, J. K., et al. 2009, ApJS, 181, 321
Gao, Y., & Solomon, P. M. 2004, ApJ, 606, 271
Greene, T. P., Wilking, B. A., Andre, P., Young, E. T., & Lada, C. J. 1994, ApJ, 434, 614
Hao, C.-N., Kennicutt, R. C., Johnson, B. D., et al. 2011, ApJ, 741, 124
Heiderman, A., Evans, N. J., II, Allen, L. E., Huard, T., & Heyer, M. 2010, ApJ, 723, 1019
Helou, G., Roussel, H., Appleton, P., et al. 2004, ApJS, 154, 253
Helou, G., Soifer, B. T., & Rowan-Robinson, M. 1985, ApJL, 298, L7
Hopkins, A. M. 2004, ApJ, 615, 209
Hughes, A., Wong, T., Ekers, R., et al. 2006, MNRAS, 370, 363
Jogee, S., Scoville, N., & Kenney, J. D. P. 2005, ApJ, 630, 837
Kennicutt, R. C., Jr. 1998a, ApJ, 498, 541
Kennicutt, R. C., Jr. 1998b, ARA&A, 36, 189
Kennicutt, R. C., Jr., Armus, L., Bendo, G., et al. 2003, PASP, 115, 928
Kennicutt, R. C., Jr., & Evans, N. J., II 2012, ARA&A, 50, 531
Kennicutt, R. C., Jr., Hao, C.-N., Calzetti, D., et al. 2009, ApJ, 703, 1672
Kinney, A. L., Bohlin, R. C., Calzetti, D., Panagia, N., & Wyse, R. F. G. 1993, ApJS, 86, 5
Kroupa, P. 2001, MNRAS, 322, 231
Kroupa, P. 2002, Sci, 295, 82
Krumholz, M. R., Dekel, A., & McKee, C. F. 2012, ApJ, 745, 69
Krumholz, M. R., Leroy, A. K., & McKee, C. F. 2011, ApJ, 731, 25
Leitherer, C., Schaerer, D., Goldader, J. D., et al. 1999, ApJS, 123, 3
Lockman, F. J. 1989, ApJS, 71, 469
Markwardt, C. B. 2009, in ASP Conf. Ser. 411, Astronomical Data Analysis Software and Systems XVIII, ed. D. A. Bohlender, D. Durand, & P. Dowler (San Francisco, CA: ASP), 251
McKee, C. F., & Ostriker, E. C. 2007, ARA&A, 45, 565
Miville-Deschênes, M.-A., & Lagache, G. 2005, ApJS, 157, 302
Mueller, K. E., Shirley, Y. L., Evans, N. J., II, & Jacobson, H. R. 2002, ApJS, 143, 469
Murphy, E. J., Braun, R., Helou, G., et al. 2006, ApJ, 638, 157
Murphy, E. J., Condon, J. J., Schinnerer, E., et al. 2011, ApJ, 737, 67
Murray, N. 2011, ApJ, 729, 133
Padgett, D. L., Rebull, L. M., Stapelfeldt, K. R., et al. 2008, ApJ, 672, 1013
Pérez-González, P. G., Kennicutt, R. C., Jr., Gordon, K. D., et al. 2006, ApJ, 648, 987
Plume, R., Jaffe, D. T., & Evans, N. J., II 1992, ApJS, 78, 505
Plume, R., Jaffe, D. T., Evans, N. J., II, Martin-Pintado, J., & Gomez-Gonzalez, J. 1997, ApJ, 476, 730
Rahman, N., Bolatto, A. D., Wong, T., et al. 2011, ApJ, 730, 72
Rebull, L. M., Stapelfeldt, K. R., Evans, N. J., II, et al. 2007, ApJS, 171, 447
Reiter, M., Shirley, Y. L., Wu, J., et al. 2011, ApJS, 195, 1
Relaño, M., Lisenfeld, U., Pérez-González, P. G., Vílchez, J. M., & Battaner, E. 2007, ApJL, 667, L141
Rieke, G. H., Alonso-Herrero, A., Weiner, B. J., et al. 2009, ApJ, 692, 556
Salim, S., Rich, R. M., Charlot, S., et al. 2007, ApJS, 173, 267
Schruba, A., Leroy, A. K., Walter, F., et al. 2011, AJ, 142, 37
Shi, Y., Helou, G., Yan, L., et al. 2011, ApJ, 733, 87

Shirley, Y. L., Evans, N. J., II, Young, K. E., Knez, C., & Jaffe, D. T. 2003, ApJS, 149, 375
Tabatabaei, F. S., Beck, R., Krause, M., et al. 2007, A&A, 466, 509
Verley, S., Corbelli, E., Giovanardi, C., & Hunt, L. K. 2009, A&A, 493, 453
Williams, M. J., Bureau, M., & Cappellari, M. 2010, MNRAS, 409, 1330
Wu, H., Cao, C., Hao, C.-N., et al. 2005a, ApJL, 632, L79
Wu, J., Evans, N. J., II, Gao, Y., et al. 2005b, ApJL, 635, L173
Wu, J., Evans, N. J., II, Shirley, Y. L., & Knez, C. 2010, ApJS, 188, 313
Yun, M. S., Reddy, N. A., & Condon, J. J. 2001, ApJ, 554, 803
Zhang, J., Hopkins, A., Barnes, P. J., et al. 2010, PASA, 27, 340
Zhu, Y.-N., Wu, H., Cao, C., & Li, H.-N. 2008, ApJ, 686, 155